JBC RESEARCH ARTICLE

Adenine base editor–mediated splicing remodeling activates noncanonical splice sites

Received for publication, May 18, 2023, and in revised form, October 15, 2023 Published, Papers in Press, November 9, 2023,
https://doi.org/10.1016/j.jbc.2023.105442

Yuanyuan Liu[1,2,‡], Qing Li[3,‡], Tong Yan[1], Haoran Chen[1], Jiahua Wang[1], Yingyi Wang[4], Yeqin Yang[5], Lue Xiang[1], Zailong Chi[1], Kaiqun Ren[2], Bin Lin[6], Ge Lin[7,8], Jinsong Li[3,4], Yong Liu[1,*], and Feng Gu[1,2,9,*]

From the [1]School of Ophthalmology and Optometry, Eye Hospital, Wenzhou Medical University, State Key Laboratory and Key Laboratory of Vision Science, Ministry of Health and Zhejiang Provincial Key Laboratory of Ophthalmology and Optometry, Wenzhou, Zhejiang, China; [2]Key Laboratory of Model Animals and Stem Cell Biology in Hunan Province, School of Medicine, Engineering Research Center of Reproduction and Translational Medicine of Hunan Province, Hunan Normal University, Changsha, China; [3]State Key Laboratory of Cell Biology, Shanghai Key Laboratory of Molecular Andrology, Shanghai Institute of Biochemistry and Cell Biology, Center for Excellence in Molecular Cell Science, Chinese Academy of Sciences, Shanghai, China; [4]School of Life Science and Technology, Shanghai Tech University, Shanghai, China; [5]School of Nursing, Zhejiang Chinese Medical University, Hangzhou, Zhejiang, China; [6]School of Optometry, Hong Kong Polytechnic University, Hong Kong, China; [7]Clinical Research Center for Reproduction and Genetics in Hunan Province, Reproductive and Genetic Hospital of CITIC-Xiangya, Changsha, China; [8]Institute of Reproductive and Stem Cell Engineering, School of Basic Medical Science, Central South University, Changsha, China; [9]Guangxiu Hospital Affiliated with Hunan Normal University (Hunan Guangxiu Hospital), Changsha, China

Reviewed by members of the JBC Editorial Board. Edited by Kirill Martemyanov

Adenine base editors (ABEs) are genome-editing tools that have been harnessed to introduce precise A•T to G•C conversion. The discovery of split genes revealed that all introns contain two highly conserved dinucleotides, canonical "AG" (acceptor) and "GT" (donor) splice sites. ABE can directly edit splice acceptor sites of the adenine (A) base, leading to aberrant gene splicing, which may be further adopted to remodel splicing. However, spliced isoforms triggered with ABE have not been well explored. To address it, we initially generated a cell line harboring C-terminal enhanced GFP (eGFP)–tagged *β-actin* (*ACTB*), in which the eGFP signal can track endogenous *β-actin* expression. Expectedly, after the editing of splice acceptor sites, we observed a dramatical decrease in the percentage of eGFP-positive cells and generation of splicing products with the noncanonical splice site. Furthermore, we manipulated *Peroxidasin* in mouse embryos with ABE, in which a noncanonical acceptor was activated to remodel splicing, successfully generating a mouse disease model of anophthalmia and severely malformed microphthalmia. Collectively, we demonstrate that ABE-mediated splicing remodeling can activate a noncanonical acceptor to manipulate human and mouse genomes, which will facilitate the investigation of basic and translational medicine studies.

Precision genome engineering involves a broad range of research and medical applications. A CRISPR-associated protein 9 (Cas9) system has been developed as a simple and efficient genome-editing method (1), which revolutionizes genomic engineering to achieve precise genome modification. Conventional Cas9 system triggers the generation of double-strand breaks that frequently lead to genome lesions and recombination (2). However, base editing is a genome-editing method that directly generates precise point mutation(s) without creating double-strand breaks, and it can minimize the off-target effect compared with CRISPR–Cas9-mediated editing (3). Two major classes of DNA base editors have been reported including cytosine base editors (CBEs) (3) and adenine base editors (ABEs) (4), which convert a C•G base pair into a T•A pair and an A•T base pair into a G•C pair, respectively. In addition, C-to-G base editors are reported for C to G conversion (5). Base editors have been successfully implemented in various organisms (6–8). However, the low efficiency of early ABEs (*i.e.*, ABE7.10) severely hamper their applications (4, 9). Recently, several high-activity variants have been identified, including ABE8e (10), ABE8s (11), and NG-ABEmax-KR from our group (12).

The discovery of split genes revealed that all introns contain two highly conserved dinucleotides, namely, canonical "AG" (splice acceptor [SA]) and "GT" (splice donor) splice sites (13). RNA splicing can splice one gene into multiple isoforms, which is a critical biological process by which pre-mRNA matures through the removal of intronic sequences resulting in the juxtaposition of exons to form mature transcripts before translation into proteins (12). RNA splicing plays an important role in organismal development and growth and even in some human diseases (14, 15). Gene mutations within the exon–intron borders can affect splicing patterns by disrupting existing splice sites, splicing regulatory sequences (intronic and exonic splicing silencers and enhancers) (16, 17), creating new ones, such as acceptor and donor sites, activating cryptic ones, or inducing the incorporation of pseudoexons (18, 19).

As ABE can convert an A•T base pair into a G•C pair, accordingly, it may potentially disrupt the SA of "AG" to "GG"

‡ These authors contributed equally to this work.
* For correspondence: Feng Gu, gufenguw@gmail.com; Yong Liu, yongliu@wmu.edu.cn.

(20), which may recapitulate human genetic disease in cellular models or animal models (9, 21). Therefore, abnormal splicing can lead to splicing remodeling (SR). However, spliced isoforms triggered with ABE have not been well explored.

In this study, we initially used ABE to disrupt the SA of *ACTB*, and we found that the expression of the target gene was modulated. Moreover, we found that noncanonical acceptor-mediated splicing was activated after editing with ABE, which was further verified in cultured cells and genetically engineered mouse models with anophthalmia and severely malformed microphthalmia. Collectively, we demonstrate that ABE-mediated SR (ABE-SR) may activate noncanonical splice sites, which may facilitate basic and translational medicine studies.

Results

Generation of C-terminal enhanced GFP–tagged β-actin *cells and SR with NG-ABEmax-KR editing*

To investigate the effects of ABE-SR, cells harboring C-terminal enhanced GFP (eGFP)–tagged *β-actin* fusion protein were generated by knocking in an eGFP at *the ACTB* gene in human embryonic kidney 293 (HEK-293) cells (Fig. 1). Thus, the eGFP signal can track endogenous *β-actin* expression. We designed sequence-specific RNA-guided Cas9 to target the stop codon of the *β-actin* gene, and the *eGFP* gene was knocked in at this *locus* (Fig. 1*A*). To select the positive colonies, *puromycin N-acetyl transferase* (*puromycin*) was included in the knock-in cassette. With the cleavage of the sequence encoding for the stop codon of *ACTB*, the expression cassette of the *eGFP*–IRES–*puromycin* encoding sequence was knocked in at this site (Fig. 1*B*). After transfection with *β-actin-eGFP*-IRES-*PURO*, the cells exhibit green fluorescence signals. One colony (HEK-*ACTIN-GFP*) was selected for further study (Fig. 1*C*).

We next studied the mRNA SR of the *ACTB* gene by editing the SA of ACTB with ABE. Five single guide RNAs (sgRNAs) were designed to edit the SA between intron 1 and intron 5 of *ACTB*, and the effects of SR were accessed by flow cytometry (Figs. 2*A* and S1). Expectedly, after editing the SA of intron 5 with NG-ABEmax-KR, the percentage of eGFP-negative cells in the total population was 59.83, compared with 25.66, 21.24, 31.22, and 39.83 at the SA of introns 1, 2, 3, and 4, respectively, and 1.25 of the negative control (Fig. 2*B*). Very similar results were obtained with ABE8e (Fig. S1). Thus, this reporter cell line could be used to assess the effects of SR by flow cytometry. To obtain the sequence insights of the editing products, RT–PCR was performed, which revealed that editing events include exon skipping (Fig. 2*C*). Surprisingly, it also includes targeted intron retention products, indicating the noncanonical splice site in the ABE-activated intron (Fig. 2*D* and Table S1). Next-generation sequencing (NGS) was harnessed for assessing editing events. The results show that the editing efficiency of ABE at the different target sites varied (Fig. 2*E*), which is generally consistent with the results *via* flow cytometry. Collectively, these results illustrate that editing splicing sites in HEK-293 cells with ABE can efficiently modulate gene expression. Most importantly, the noncanonical splice site can be activated after editing (Figs. S2 and S3).

Generation of mouse disease model of anophthalmia and severely malformed microphthalmia with splicing modeling

To test whether ABE-mediated splicing could be harnessed for the efficient generation of mouse disease models, an sgRNA was designed to target c.840-2 of the *Peroxidasin* (*Pxdn*) gene (Fig. 3*A*), an essential gene for eye development and function (22, 23). The human and mouse *Pxdn* genes were aligned, revealing that it is highly conserved (24). Because *Pxdn* mutations were frequently reported in immunoglobulin-like domain and heme peroxidase domain–encoded sequence, which is upstream of exon 9 (exon 9 has 34 nt), manipulating the SA of intron 9 of mouse *Pxdn* may cause an out of frame of *Pxdn* (25).

To generate a disease model, we designed an sgRNA to convert the SA "AG" of *Pxdn* to "GG" (Table S2). Genotyping analysis of the engineered mice was performed by PCR and Sanger sequencing (Fig. 3*B*). Not surprisingly, three point mutations of "A" to "G" mutations were introduced. To simplify the genotyping steps, a restriction fragment length polymorphism method was developed. Specifically, the 283-bp fragment harboring the edited site was amplified by PCR, which may be cleaved by Tsp45I restriction enzyme with the introduction of mutation (Fig. 3*C*). Fragments digested with Tsp45I amplified from the mutant mice can be cut into 140-bp and 143-bp parts, whereas the fragments from WT mice ($Pxdn^{+/+}$, WT) were resistant to the digestion (Fig. 3*D*). Then, we sought to identify whether the splicing was affected. The sequencing results of the RT–PCR products showed that partial intron 8 (185 bp) was transcribed because of the activation of the noncanonical splice site in the ABE-triggered intron (Fig. 3*E*). It resulted in partial intron retention and then an out-of-frame mutation of the *Pxdn* gene (Fig. 3*F*). As we expected, *Pxdn* protein cannot be detected in the homozygous mice with Western blotting (Fig. 3*G*). These results revealed that with ABE-mediated editing in mice, the splicing could be remodeled under the activation of a noncanonical splice site, which then affects the expression of the edited gene(s).

Mice with splicing site mutations recapitulate clinical manifestations

The aforementioned results showed that at the genome level, *Pxdn* was once mutated, and its RNA sequence was subsequently changed. Thus, we tested whether it could recapitulate human diseases, that is, anophthalmia and severely malformed microphthalmia. *Pxdn* is a heme-containing peroxidase that is secreted into the extracellular matrix. It is involved in extracellular matrix formation and may be involved in the physiological and pathological fibrogenic response in some fibrotic viscera (26). In addition, a high *Pxdn* expression is observed in several human tissues, such as the heart, spleen, kidney, and lung (27).

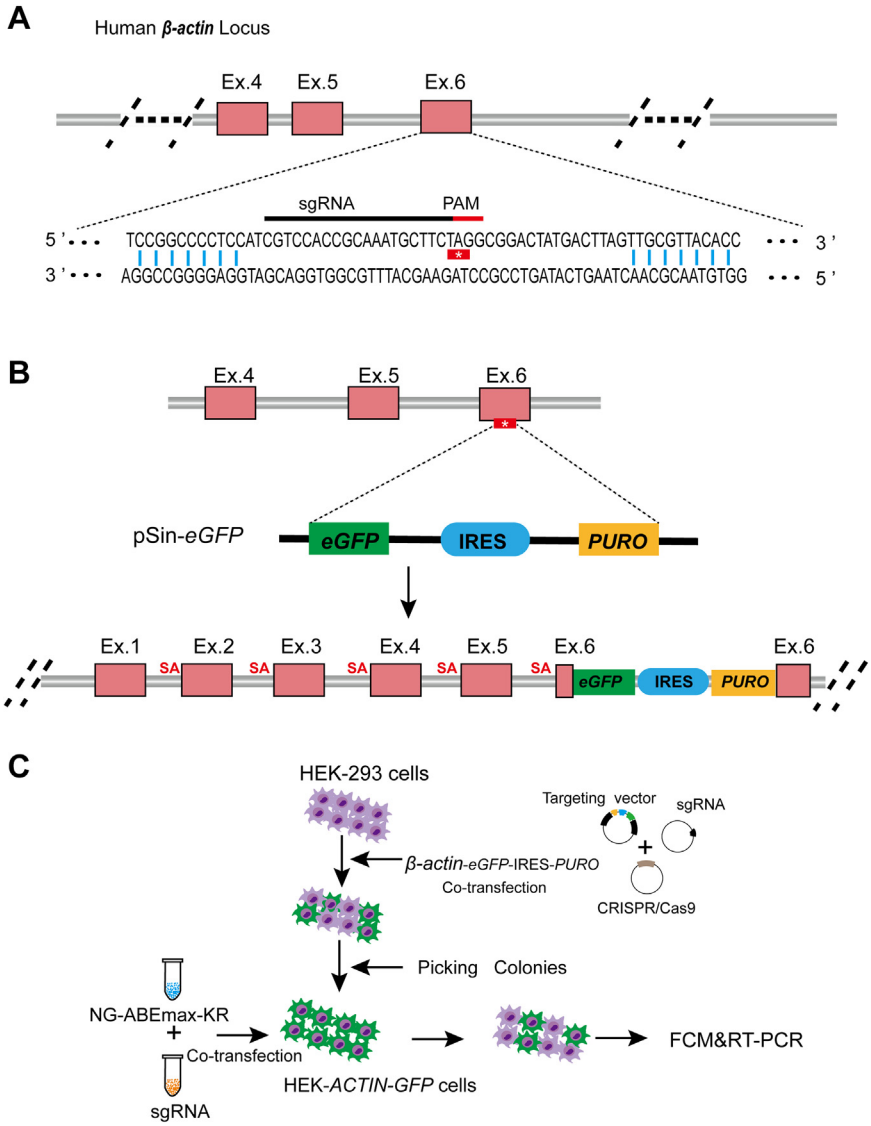

Figure 1. Schematic representation of the knock-in eGFP cassette at the human *β-actin* locus. *A*, target sequences were selected for the CRISPR/Cas9-mediated cleavage. *B*, partial fragments of the pSin-*eGFP* plasmid were inserted at the termination codon of exon 6 of the *β-actin (ACTB)* gene to generate an HEK-*ACTIN-GFP* cell line harboring *eGFP*-IRES-*PURO*-tagged cassette. Splice acceptors (SAs) of the *β-actin* were highlighted in *red*. *C*, protocol of using HEK-*ACTIN-GFP* to access the editing efficiency of ABE. Cas9, CRISPR-associated protein 9; eGFP, enhanced GFP; Ex., exon; FCM, flow cytometry analysis; HEK, human embryonic kidney cell line.

Compared with the WT, adult *Pxdn* mutant mice (heterozygotes and homozygotes) did not exhibit any apparent difference in size and weight (Fig. 4*A*), as well as most organs, including the brain, heart, lung, spleen, kidney, and liver, except for the eyes (Fig. 4*B*). Homozygous mice had small eyes. At approximately 3 weeks, the contrast of eyes will become more noticeable. In addition, hair color was changed, and in homozygous mice (n = 26), the tail color was white in two-third location of the tip at a frequency of approximately 96.2% (Fig. 4*A*) (24, 28). Compared with the WT and heterozygotes, the homozygous mice exhibited severe abnormalities in the external appearance of the eyes (Fig. 4*C*). Closed eyelids, corneal opacification, and serious cataracts in homozygous mice are manifestations of corresponding patients (23). Unsurprisingly, heterozygous and WT mice have normal eyelids, corneal, lens, retinal structures, and visual functions (Fig. 4*D* and S4). Taken together, these results demonstrate that *Pxdn* with the splicing site mutation can recapitulate the clinical manifestations of patients.

Extremely disorganized eye structure of Pxdn*-null mice*

To further determine histological abnormalities, paraffin-embedded eye sections were used for H&E staining (Fig. 4*E*). Histological analysis of the eye tissues of homozygote mice showed an extremely serious abnormality. Complete lens loss or residual traces were observed. Disorganized retinal structures such as the retinal folds or rosette-like structures, retinal retraction, and retinal hypoplasia were also observed. In addition, the optic nerve and each layer of the retina were notably thinner in mutants than in WT (Fig. 4*F*). Therefore, these data indicate that *Pxdn* is important in the organization

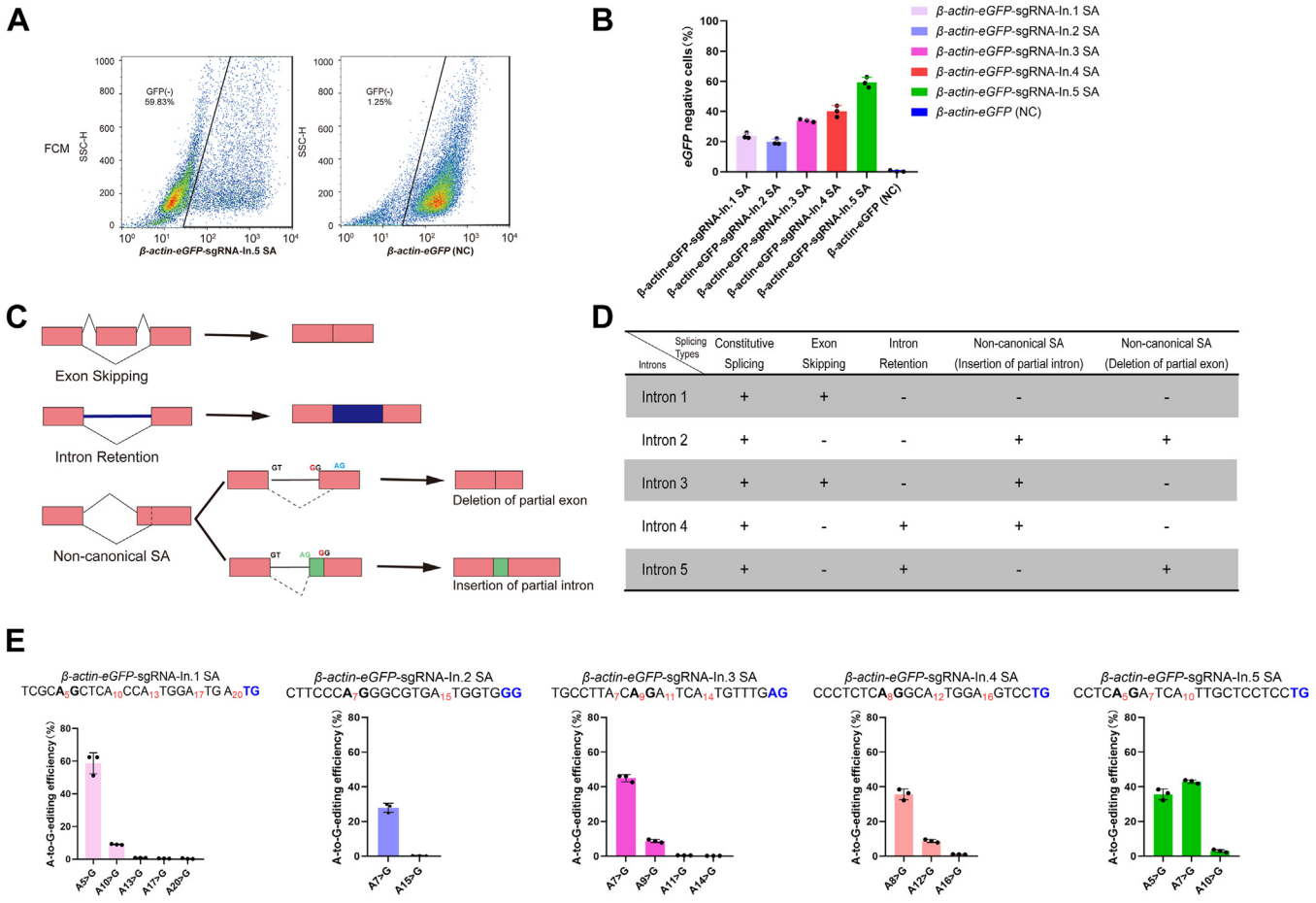

Figure 2. ABE-mediated splicing remodeling at the *ACTB (β-actin)* locus. *A*, flow cytometric assay results of editing splicing acceptor (SA) of *ACTB* intron 5 (In.5) in HEK-*ACTIN-GFP* cells. *B*, SA editing decreases eGFP expression with different sgRNAs (target SA of introns 1–5). Data are shown as the average mean ± SD (n = 3 independent experiments). *C*, illustration of different splicing products from RT–PCR analysis. *D*, summary of splicing products from targeting different SAs of introns. + represents the existence of the splicing products. *E*, the editing efficiency of targeting different SAs assessed with NGS. Each A base, PAM sequences, and SA ("AG") are highlighted with *red*, *blue*, and in *bold*, respectively. The target sequence information was provided in the supporting information. Error bars indicate mean ± SD (n = 3 independent experiments). *$p < 0.05$, **$p < 0.01$, ***$p < 0.001$, and ****$p < 0.0001$ by Student's unpaired two-sided *t* test. ABE, adenine base editor; eGFP, enhanced GFP; HEK, human embryonic kidney cell line; NGS, next-generation sequencing; sgRNA, single guide RNA.

of eyeball structures and lens development during eye development.

Identifying the causative base mutation affecting Pxdn *splicing*

Owing to bystander mutations triggered with ABE, three point mutations in the engineered mice were noted: [c. 840-4A > G (labeled with A3 > G); c. 841A > G, A8 > G; and c. 840-2A > G, A5 > G]. Then we sought to know which mutation(s) affects the splicing. To address it, we generated vectors carrying the *Pxdn* fragment harboring different single mutation fused with eGFP encoding sequence, respectively. Fluorescence images showed that, compared with the eGFP vector control, WT, the (A3 > G) and (A8 > G) groups exhibited slightly low green fluorescence signal, whereas the A5 > G group almost abolished green fluorescence (Fig. 5*B*), which was further confirmed by flow cytometry (Fig. 5*C*). These results showed that a single-base mutation at the splicing site can seriously affect splicing (Fig. 5*D*). Taken together, these results showed that single base of splicing site editing triggered by ABE can manipulate gene expression.

Discussion

Increasing evidence shows that human disease genes harbor mutations (intron, exon, and splicing sites) that affect pre-mRNA splicing (4, 29, 30). To recapitulate diseases, precision gene editing of splicing-related sequences is required. Thus far, ABE and CBE have been harnessed for gene manipulation for splicing modulation (31). Compared with CBEs, ABEs have higher fidelity in mouse embryos (21, 32–35). Thus, ABEs may possess an advantage over the other editors for splicing engineering. To demonstrate the performance of ABE-triggered SR, we knocked in an eGFP reporter gene at the C-terminal region of the *β-actin* gene for tracking the endogenous *β-actin* expression (Fig. 1). After the disruption of the SA, we observed a decrease in the percentage of eGFP-positive cells and the activation of a noncanonical acceptor (Fig. 2*B*). Moreover, we generated a disease model through the microinjection of ABE

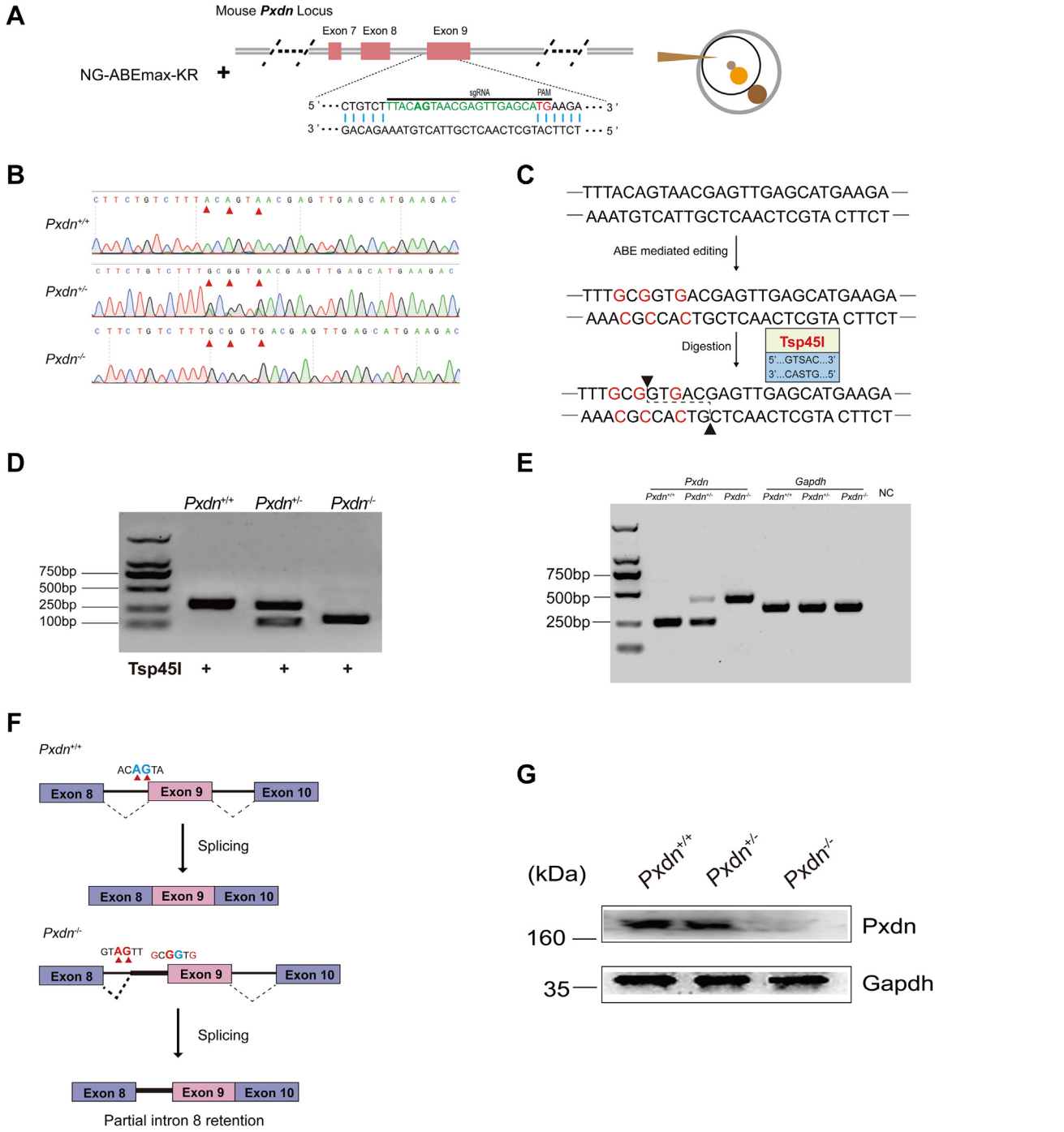

Figure 3. Activation of *a Pxdn* noncanonical acceptor to generate a mouse disease model. A schematic of NG-ABEmax-KR in mouse embryos *via* zygote intracytoplasmic injection (target and PAM sequence were highlighted in *green* and *red*, respectively). *B*, Sanger sequencing results of the mice harboring *Pxdn* knocked-in point mutations. *C*, the mutant sequence has a Tsp45I recognition site. *D*, genotyping of the mice (140 bp and 143 bp for mutant mice, 283 bp for the WT mouse [$Pxdn^{+/+}$]). *E*, RT–PCR analyses of *Pxdn* expression in eye tissues. *Gapdh* was used as a control. *F*, activated noncanonical acceptor for splicing. The partial intron is retained in the novel splicing isoform. Splice acceptor site was highlighted with *red triangle*. *G*, Western blot analysis of *Pxdn* expression. The lung tissue of the mice was selected for the analysis. Gapdh was used as a loading control. *Pxdn*, *peroxidasin* gene.

and sgRNA to target *Pxdn* in mouse zygotes (Fig. 3*A*). A-to-G conversion was achieved at the SA of the *Pxdn* intron 8 (Fig. 3*F*). With additional sequence analysis, we found that the activation of the noncanonical acceptor is responsible for the SR and generation of the mouse disease model. The *Pxdn* mutant mice exhibit a typical phenotype of anterior segment dysgenesis, anophthalmia, or severe microphthalmos (Fig. 4). Compared with the traditional knock-out animal disease model, ABE-mediated splicing engineering to generate a disease model only possesses base conversions, no indels, and proximal mutations (21). It has an advantage for preclinical therapy and recapitulating clinical mutations of patients harboring splicing mutations. These results illustrated the versatility of ABE, which confers it as a powerful genetic tool

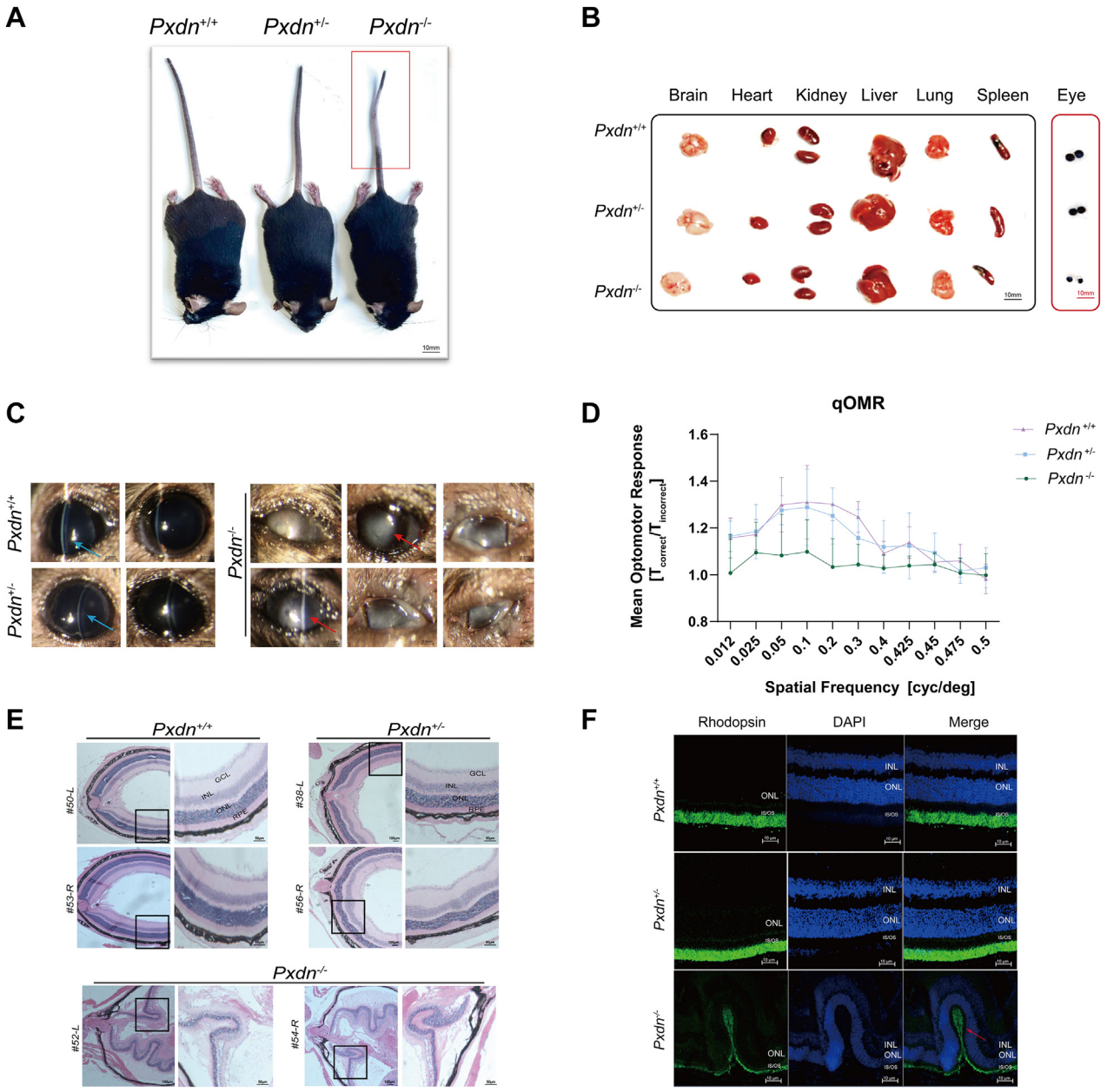

Figure 4. Eye structure and vision function of *Pxdn* mutant mice. *A*, representative photograph of $Pxdn^{+/+}$ (WT, n = 20), $Pxdn^{+/-}$ (heterozygous, n = 24), and $Pxdn^{-/-}$ (homozygous, n =26) mice (3 months old). *B*, comparison of mouse organs (approximately 6 months old). The eyeball is highlighted in the *red box*. *C*, representative morphology of the eyes in WT, heterozygous, and homozygous mice. Compared with WT (n = 38) or heterozygous mice (n = 43), completely or nearly closed eyelids were observed in the homozygous mice (n = 40). Corneal transparency and corneal opacity were highlighted with *blue* and *red arrows*, respectively. *D*, visual acuity was measured by PhenoSys qOMR (n = 18, $^{****}p < 0.0001$). *E* and *F*, histological analysis of *Pxdn* homozygous mice. Representative histological data and retinal immunofluorescence staining results of the eye tissues of the WT, heterozygous, or homozygous mice (3–6 months old). Paraffin-embedded eye sections were stained with H&E. Scale bar represents 200 μm. The eye tissues of heterozygous mice (n = 16, male = 8, female = 8) displayed normal anterior segments similar to that of WT mice (n = 18, male = 9, female = 9), whereas the eye tissues of the homozygous mice (n = 12, male = 6, female = 6) exhibited extremely disorganized eye structures or no eyeball structure. *Pxdn*, *peroxidasin* gene; qOMR, quantitative OMR.

for SR, including exon skipping, exon inclusion, switching between mutually exclusive exons, selection of alternative splice sites, retention of short introns, and activation of noncanonical acceptors (36). Because of the homozygous mutations of genes (*i.e.*, *Pxdn*) for the most of human genetic diseases, direct editing of the SA sites to convert the dominant model to the recessive model *via* inactivation may be an alternative approach to treating dominant genetic diseases.

The bystander effect of ABE precludes its applications in human gene therapy and precise disease modeling. To address it, we identified a novel ABE variant (NG-ABE9e), which has nine mutations (37), compared with ABEmax. NG-ABE9e demonstrates a substantially higher activity than NG-ABEmax and significantly lower bystander editing than NG-ABE8e *in vitro* in cells, animals, and plants. Recently, Yang *et al.* (38) reported an adenine transversion base editor, AYBE,

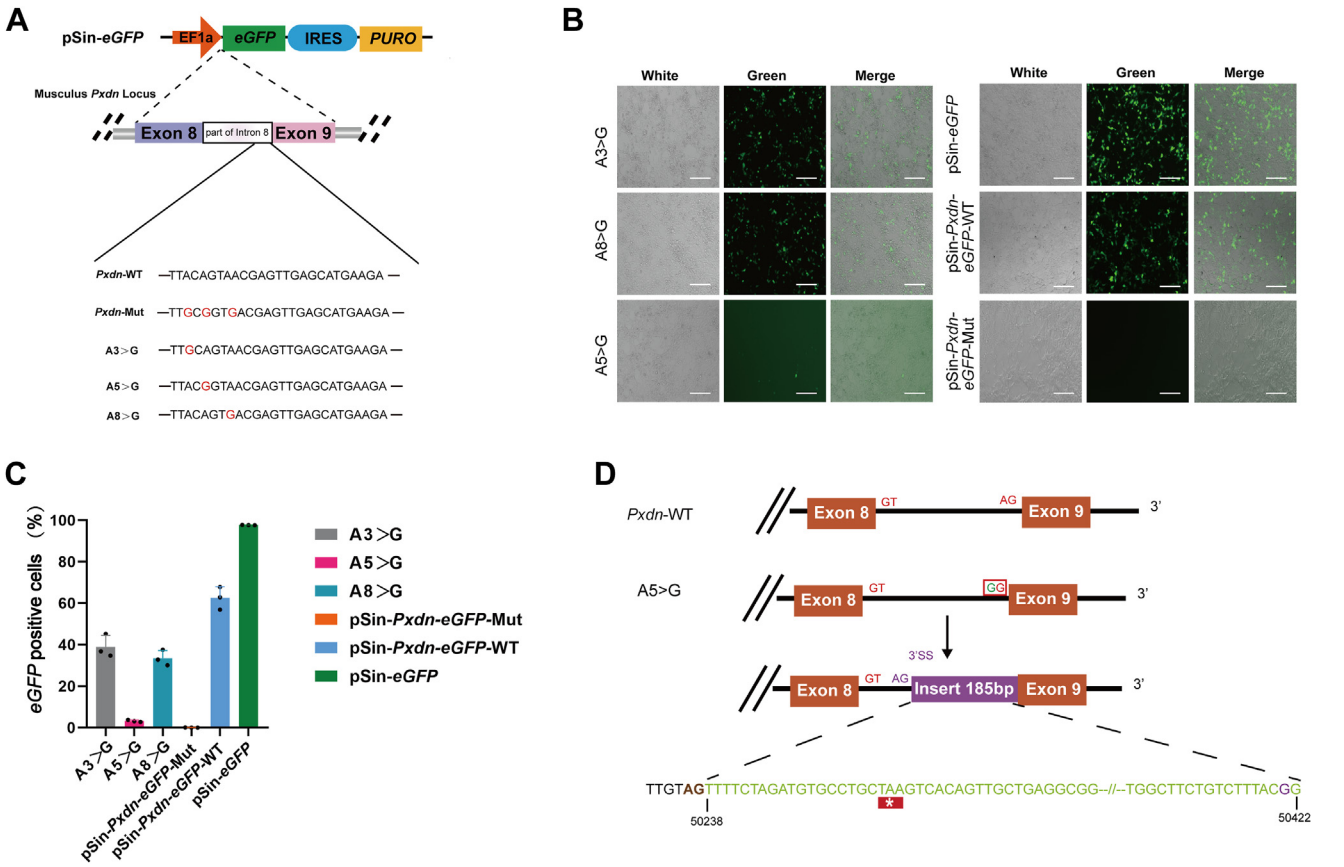

Figure 5. Mapping the key base of the point mutations modulating splicing in *Pxdn*. *A*, generation of vectors harboring A3, A5, and A8 of A > G mutations. Sequence of mouse exons 8 and 9 and some intron 8 was inserted and fused with *eGFP* gene. *B* and *C*, image of the cells under the fluorescence microscope (*B*) and flow cytometry assay results (*C*) of HEK-293 cells transfected with plasmids of pSin-*Pxdn*-eGFP as backbone, including WT, Mut(mutant), three single mutants (A3 > G), (A5 > G), and (A8 > G), respectively. The cells exhibit *green* fluorescence harboring the partial sequence of WT *Pxdn*. Flow cytometry assay results showed that the A5 > G mutation abolished the eGFP expression, indicating the key role for the splicing remodeling. Data are shown as the average mean ± SD (n = 3 independent experiments). Scale bar represents 10 μm. *D*, schematic of A5 > G mutation leading to activation of noncanonical acceptor for splicing. The transcript harboring 185-bp intron was generated, which has a premature termination codon. eGFP, enhanced GFP; HEK-293, human embryonic kidney 293 cell line; *Pxdn*, *peroxidasin* gene.

for A-to-C and A-to-T transversion editing in mammalian cells by fusing an ABE with hypoxanthine excision protein *N*-methylpurine DNA glycosylase. An unnatural cytosine deaminase evolved from adenine deaminase TadA-8e was developed, which enables highly efficient and accurate C-to-G or C-to-T conversions, named Td-CGBE and Td-CBE (39). These tools provided a complementary toolkit to the current base editor repertoire for splicing modeling.

Based on our results, how to design an ABE-SR to activate the noncanonical acceptor is still elusive. We predicted the spliced sequence in available websites, and we cannot find the exact transcripts generated from the noncanonical acceptor. We acknowledge that so far, the splicing mechanisms that depend on exonic signals may require further elucidation. Recently, it has been reported that the cell type–specific impact of somatic mutations on RNA splicing could be revealed *via* GoT-Splice (40). Thus, ABE-mediated therapeutic approaches to treat certain genetic diseases or disease modeling may be optimized and further explored.

In conclusion, our study demonstrated that ABE-SR can activate a noncanonical acceptor to manipulate human and mouse genomes, which will shed light on new avenues of research for precise gene editing in disease modeling and gene therapy.

Experimental procedures

Plasmid construction

The genomic DNAs from HEK-293 cells were used as the template for PCR amplification using specific primers. The PCR products were subsequently purified (654 bp and 597 bp from the upstream and downstream of the ACTB termination codon as homologous arms). About 1988 bp of *eGFP*-IRES-*PURO* fragment was amplified from pSin-eGFP plasmid, and products were inserted into the vector pJET1.2 (CloneJET PCR Cloning Kit; Thermo Fisher Scientific) (Table S3). The ligated products were transformed into *Escherichia coli.* The corresponding plasmids were isolated and sequenced on an ABI PRISM 3730 DNA Sequencer. Fragments harboring *Pxdn* point mutation(s) were inserted into the pSin-eGFP plasmid. Different sgRNAs were inserted into the backbone of pJet-U6 using BbsI digestion (Table S4).

ABE–mediated splicing remodeling

Cells and cell culture

HEK-293 cells were obtained from American Type Culture Collection (catalog no.: CRL1573). HEK-293 cells harboring C-terminal eGFP tag beta-actin are named HEK-*ACTIN-GFP* cells. HEK-293 cells were grown at 37 °C in 5% CO_2 in Dulbecco's modified Eagle's medium (Life Technologies) supplemented with 10% heat-inactivated fetal bovine serum and penicillin/streptomycin. HEK-*ACTIN-GFP* cells were cultured with puromycin (concentration of 1 μg/ml).

Transfection protocol, genomic DNA extraction, images, and flow cytometry analysis

For HEK-*ACTIN-GFP* cell screening experiments, HEK-293 cells were seeded at 0.9 × 10^5 cells per well on 24-well plates in Dulbecco's modified Eagle's medium. About 24 h after seeding, cells were cotransfected with 200 ng pJet-beta-actin-eGFP-*IRES-PURO* plasmids, 100 ng sgRNA expression plasmids, 200 ng px330 plasmids, and 1.5 μl TurboFect Transfection Reagent (Thermo Fisher Scientific). The medium was changed at 24 h post-transfection. The cells were cultured with the treatment of puromycin. For experiments using HEK-*ACTIN-GFP* to compare the editing activity of various sgRNA, the cells were seeded at 0.9 × 10^5 cells per well on 24-well plates in the presence of puromycin. About 24 h after seeding, cells were cotransfected with 200 ng ABE plasmids, 100 ng sgRNA expression plasmids, and 1.5 μl TurboFect Transfection Reagent. Genomic DNA extraction of cells is subsequently performed using a genome extraction kit (Vazyme). Images were obtained at 24 and 48 h (results are shown in Fig. 5*B*) by fluorescence microscope (Leica), and cells were collected at 48 h post-transfection. The flow cytometry protocol was described previously (41). Specifically, eGFP efficiency was assessed *via* FACSAria II (BD Biosciences), and the representative flow cytometry data are summarized in Fig. S1*A*.

NGS

The genomic region flanking the sgRNA target site was amplified with TransStart FastPfu DNA polymerase (TransGen Biotech) using site-specific primers in the first-round PCR. For the second step of PCR amplification, we fixed the barcodes, index, and adaptor sequences to the first-step PCR amplification products. The second-step PCR amplification products were purified and pooled and subsequently subjected to paired-end read sequencing using the Hiseq-PE150 strategy at Novogene. Finally, open-sourced "CRISPResso" software (version 1.0.10; https://github.com/pinellolab/CRISPResso2) was used to analyze the status of base editing. The oligonucleotide sequences for NGS are listed in Tables S5 and S6.

Mice

Mice were generated as previously described by us (10–12). All animals were treated in accordance with protocols approved by the School of Ophthalmology and Optometry, Eye Hospital of Wenzhou Medical University Animal Ethics Committee. The *Pxdn*$^{-/-}$ mice used in this study were generated by ABE (Table S7). Mice used in this study were either male or female of 4 weeks, 2 months, 3 months, 6 months, 9 months, or 12 months of age.

In vitro *transcription*

The mRNA transcriptional templates of NG-ABEmax-KR were amplified by PCR using Phanta Max Super-Fidelity DNA Polymerase (Vazyme), purified by the Universal DNA Purification Kit (TIANGEN). Then it was transcribed using the mMACHINE T7 ULTRA transcription Kit (Invitrogen) following the manufacturer's instruction. The transcriptional template of *Pxdn*-sgRNA was amplified from Px330-mCherry plasmids (42) (Addgene #98750) and transcribed *in vitro* using the MEGAshortscript T7 kit (Invitrogen) following the manufacturer's instructions. mRNA and sgRNA were subsequently purified with MEGAclear Transcription Clean-Up Kit (Invitrogen) and then resuspended in RNase-free water.

Microinjection and embryo transfer

The mixture of NG-ABEmax-KR mRNA (100 ng/μl) and sgRNA (100 ng/μl) was diluted in RNase-free water, centrifuging at 4 °C, 13,400*g* for 10 min, and then injected into the cytoplasm of zygotes harvested from B6D2F1 females (mated with C57BL/6J males) using a micromanipulator (Olympus) and a FemtoJet microinjector (Eppendorf). The injected embryos were cultured in Embryo Max KSOM Medium (Sigma–Aldrich) for 24 h to the two-cell embryos. The two-cell embryos were transferred into the oviducts of recipients at 0.5 days postcoitum. Recipient mothers delivered pups at 19.5 days postcoitum.

Genotyping

Genomic DNAs were isolated from the toe tissues of each mouse using a FastPure Blood/Cell/Tissue/Bacteria DNA Isolation Mini Kit (Vazyme). The PCR products were digested and visualized by agarose gel electrophoresis. The primers used for mice genotyping identification in this study are listed in Table S8.

RT–PCR analyses

Expression of *ACTB* and *Pxdn* in the cells and tissues were confirmed by RT–PCR analysis. Total RNA was extracted from the cells and tissues with Trizol reagent (Thermo Fisher). The primers set for *ACTB*, *Pxdn*, and GAPDH were found in Table S9. PCR amplification for *ACTB* and *Pxdn* mRNA expression was done under the following conditions: 95 °C for 5 min, followed by 30 to 35 cycles of 30 s at 95 °C, 30 s at 56 to 60 °C and 30 s at 72 °C, and last 72 °C for 10 min. The PCR products were loaded in an agarose gel (1.5%), and electrophoresis was performed as standard protocol. The different bands of PCR products in the electrophoresis were subsequently purified with gel purification, and then partial purified products were inserted into the vector pJET1.2 (CloneJET PCR Cloning Kit; Thermo Fisher Scientific). The ligated products were transformed into *E. coli*. The corresponding plasmids were isolated and sequenced on an ABI PRISM 3730 DNA

Sequencer. After the sequence information of each band (PCR products) was obtained, remaining purified products or raw PCR products (there is only one band in the former electrophoresis) were reloaded for the electrophoresis.

Slit lamp observation and quantitative optomotor response

In order to avoid the influence of anesthetic drugs on the corneal transparency of mice, mice were examined with a slit lamp in the awake state. We examined the anterior segment and part of the fundus after mydriasis, including eyelid, cornea, sclera, iris, lens, and vitreous body.

Optomotor response (OMR) was used to assess visual function. To evoke OMR, mice watched a defined pattern rotating within a cylinder. Stimulus-correlated head movements were quantified to determine visual thresholds (43, 44). The PhenoSys qOMR (quantitative OMR) is a unique system that automatically measures OMR with minimal experimenter effort. It uses a virtual stimulation sphere that continuously aligns with the animal's head position. Based on real-time head tracking, qOMR measurements were performed automatically and objectively. The OMR was determined and quantified by calculating the ratio of the total amount of time (converted to the sum of frames in the algorithms), and the animal head moved in the stimulus and in the opposite direction ($T_{correct}$/$T_{incorrect}$, thereafter named OMR) as conventionally used. Mice performed qOMR best at a spatial frequency of 0.1 to 0.2 cycles per degree (45). When the animal was unable to perceive the stimulus, it moved less, leading to the mean OMR value lose or equal to 1.0.

Optical coherence tomography and electroretinography

We anesthetized mice with an intraperitoneal injection of 0.5% pentobarbital sodium. The pupils were dilated with tropicamide phenylephrine eye drops. Levofloxacin eye drops were dropped on the mice cornea to delay the whitening of the mice cornea and tear film rupture. Optical coherence tomography scans were taken using the Micron IV Optical coherence tomography. We performed electroretinograph analysis using Germany Roland q450sc UV electrophysiological detection. The detailed protocol is described in our previous study (46).

Paraffin sections and H&E staining

The mice were sacrificed, and the muscle tissues around the eyeballs were stripped with tweezers under the stereofiberscope. The cornea was poked with a needle of 1 ml syringe and fixed in the eyeball fixation solution for 1 week. The fixed eyeballs were placed in the embedding box and dehydrated on the automatic tissue dehydrator (dehydrated according to the standard procedure), which were further cut into 5 μm sections using a microtome (Leica BIOCUT; Wetzlar). The paraffin sections and H&E staining were performed as standard protocol (43).

Retinal immunofluorescence

The sections (5 mm) were incubated with H&E. Anti-rhodopsin (Merck, mouse monoclonal) was used. Bound primary antibody was detected with Alexa 594-conjugated donkey antimouse immunoglobulin G (H + L) secondary antibody (Invitrogen), and the nuclei were counterstained with 4′,6-diamidino-2-phenylindole (Invitrogen). Immunofluorescence images were captured on a Zeiss confocal microscope.

Western blot analysis

The Western blotting protocol was described previously (41). Isolated lung tissues or cultured cells were lysed in commercially purchased radioimmunoprecipitation assay lysis buffer (Beyotime; catalog no.: P0013B). The primary antibodies used for mice and cells in this study are listed in Table S10. Polyvinylidene difluoride membranes were incubated with a horseradish peroxidase–linked secondary antibody, and bands were visualized using gel documentation system (Bio-Rad).

Statistical analysis

All groups of experimental mice grew and developed in the same healthy state. Numerical values and graphs are displayed as mean ± SEM unless otherwise stated. Once significance was confirmed, to ascertain significance between each group, GraphPad Prism (version 8; GraphPad Software, Inc), version 8, was used. The p values of < 0.05 were considered statistically significant. The following is used to state significance $^{*}p < 0.05$, $^{**}p < 0.01$, $^{***}p < 0.001$, or $^{****}p < 0.0001$.

Data availability

All data associated with this study are available within the article itself and its supporting information file. The data that support the findings of this study are available in the supporting information. The deep sequencing data are available at the National Center for Biotechnology Information Sequence Read Archive (https://www.ncbi.nlm.nih.gov/sra/) under BioProject PRJNA1028112 (SUB13901426; sample accession number: SAMN 37811767); raw data are available upon request from the corresponding author (F. G.).

Supporting information—This article contains supporting information.

Acknowledgments—We thank our group members for technical assistance. This work was supported by grants from the Natural Science Foundation of China (grant no.: 82271910), The Research Team for Reproduction Health and Translational Medicine of Hunan Normal University (grant no.: 2023JC101).

Author contributions—Y. L., Q. L., Y. L., and F. G. conceptualization; Y. L., Q. L., and T. Y. methodology; Y. L., Q. L., and Y. W. software; T. Y. and Y. W. validation; Y. L., Q. L., T. Y., Y. Y., and G. L. formal analysis; Y. L., Q. L., H. C., J. W., L. X., Z. C., B. L., and J. L. investigation; J. W., Y. L., and F. G. resources; T. Y. and K. R. data curation; Y. L. and Q. L. writing–original draft; Y. L. and F. G. writing–review & editing; H. C., Y. Y., L. X., Z. C., K. R., B. L., G. L., and J. L. visualization; J. L., Y. L., and F. G. supervision; Y. L. and F. G. funding acquisition.

Funding and additional information—Q. L. gratefully acknowledges the support of the Sanofi Scholarship Program.

Conflict of interest—The authors declare that they have no conflicts of interest with the contents of this article.

Abbreviations—The abbreviations used are: ABE, adenine base editor; ABE-SR, ABE-mediated SR; Cas9, CRISPR-associated protein 9; CBE, cytosine base editor; eGFP, enhanced GFP; HEK-293, human embryonic kidney 293 cell line; NGS, next-generation sequencing; OMR, optomotor response; Pxdn, peroxidasin gene; qOMR, quantitative OMR; SA, splice acceptor; sgRNA, single guide RNA; SR, splicing remodeling.

References

1. Cong, L., Ran, F. A., Cox, D., Lin, S., Barretto, R., Habib, N., *et al.* (2013) Multiplex genome engineering using CRISPR/Cas systems. *Science* **339**, 819–823
2. Kosicki, M., Tomberg, K., and Bradley, A. (2018) Repair of double-strand breaks induced by CRISPR-Cas9 leads to large deletions and complex rearrangements. *Nat. Biotechnol.* **36**, 765–771
3. Komor, A. C., Kim, Y. B., Packer, M. S., Zuris, J. A., and Liu, D. R. (2016) Programmable editing of a target base in genomic DNA without double-stranded DNA cleavage. *Nature* **533**, 420–424
4. Gaudelli, N. M., Komor, A. C., Rees, H. A., Packer, M. S., Badran, A. H., Bryson, D. I., *et al.* (2017) Programmable base editing of A*T to G*C in genomic DNA without DNA cleavage. *Nature* **551**, 464–471
5. Kurt, I. C., Zhou, R., Iyer, S., Garcia, S. P., Miller, B. R., Langner, L. M., *et al.* (2021) CRISPR C-to-G base editors for inducing targeted DNA transversions in human cells. *Nat. Biotechnol.* **39**, 41–46
6. Porto, E. M., Komor, A. C., Slaymaker, I. M., and Yeo, G. W. (2020) Base editing: advances and therapeutic opportunities. *Nat. Rev. Drug Discov.* **19**, 839–859
7. Levy, J. M., Yeh, W. H., Pendse, N., Davis, J. R., Hennessey, E., Butcher, R., *et al.* (2020) Cytosine and adenine base editing of the brain, liver, retina, heart and skeletal muscle of mice via adeno-associated viruses. *Nat. Biomed. Eng.* **4**, 97–110
8. Newby, G. A., Yen, J. S., Woodard, K. J., Mayuranathan, T., Lazzarotto, C. R., Li, Y., *et al.* (2021) Base editing of haematopoietic stem cells rescues sickle cell disease in mice. *Nature* **595**, 295–302
9. Kluesner, M. G., Lahr, W. S., Lonetree, C. L., Smeester, B. A., Qiu, X., Slipek, N. J., *et al.* (2021) CRISPR-Cas9 cytidine and adenosine base editing of splice-sites mediates highly-efficient disruption of proteins in primary and immortalized cells. *Nat. Commun.* **12**, 2437
10. Richter, M. F., Zhao, K. T., Eton, E., Lapinaite, A., Newby, G. A., Thuronyi, B. W., *et al.* (2020) Phage-assisted evolution of an adenine base editor with improved Cas domain compatibility and activity. *Nat. Biotechnol.* **38**, 883–891
11. Gaudelli, N. M., Lam, D. K., Rees, H. A., Sola-Esteves, N. M., Barrera, L. A., Born, D. A., *et al.* (2020) Directed evolution of adenine base editors with increased activity and therapeutic application. *Nat. Biotechnol.* **38**, 892–900
12. Fu, J., Li, Q., Liu, X., Tu, T., Lv, X., Yin, X., *et al.* (2021) Human cell based directed evolution of adenine base editors with improved efficiency. *Nat. Commun.* **12**, 5897
13. Pan, Q., Shai, O., Lee, L. J., Frey, B. J., and Blencowe, B. J. (2008) Deep surveying of alternative splicing complexity in the human transcriptome by high-throughput sequencing. *Nat. Genet.* **40**, 1413–1415
14. Montes, M., Sanford, B. L., Comiskey, D. F., and Chandler, D. S. (2019) RNA splicing and disease: animal models to therapies. *Trends Genet.* **35**, 68–87
15. Bradley, R. K., and Anczukow, O. (2023) RNA splicing dysregulation and the hallmarks of cancer. *Nat. Rev. Cancer* **23**, 135–155
16. Wang, Y., Ma, M., Xiao, X., and Wang, Z. (2012) Intronic splicing enhancers, cognate splicing factors and context-dependent regulation rules. *Nat. Struct. Mol. Biol.* **19**, 1044–1052
17. Wang, Z., Rolish, M. E., Yeo, G., Tung, V., Mawson, M., and Burge, C. B. (2004) Systematic identification and analysis of exonic splicing silencers. *Cell* **119**, 831–845
18. Kornblihtt, A. R., Schor, I. E., Allo, M., Dujardin, G., Petrillo, E., and Munoz, M. J. (2013) Alternative splicing: a pivotal step between eukaryotic transcription and translation. *Nat. Rev. Mol. Cell Biol.* **14**, 153–165
19. De Conti, L., Baralle, M., and Buratti, E. (2013) Exon and intron definition in pre-mRNA splicing. *Wiley Interdiscip. Rev. RNA* **4**, 49–60
20. Matsoukas, I. G. (2018) Commentary: programmable base editing of A.T to G.C in genomic DNA without DNA cleavage. *Front Genet.* **9**, 21
21. Lee, H. K., Willi, M., Miller, S. M., Kim, S., Liu, C., Liu, D. R., *et al.* (2018) Targeting fidelity of adenine and cytosine base editors in mouse embryos. *Nat. Commun.* **9**, 4804
22. Peterfi, Z., and Geiszt, M. (2014) Peroxidasins: novel players in tissue genesis. *Trends Biochem. Sci.* **39**, 305–307
23. Khan, K., Rudkin, A., Parry, D. A., Burdon, K. P., McKibbin, M., Logan, C. V., *et al.* (2011) Homozygous mutations in PXDN cause congenital cataract, corneal opacity, and developmental glaucoma. *Am. J. Hum. Genet.* **89**, 464–473
24. Yan, X., Sabrautzki, S., Horsch, M., Fuchs, H., Gailus-Durner, V., Beckers, J., *et al.* (2014) Peroxidasin is essential for eye development in the mouse. *Hum. Mol. Genet.* **23**, 5597–5614
25. Shi, R., Cao, Z., Li, H., Graw, J., Zhang, G., Thannickal, V. J., *et al.* (2018) Peroxidasin contributes to lung host defense by direct binding and killing of gram-negative bacteria. *PLoS Pathog.* **14**, e1007026
26. Medfai, H., Khalil, A., Rousseau, A., Nuyens, V., Paumann-Page, M., Sevcnikar, B., *et al.* (2019) Human peroxidasin 1 promotes angiogenesis through ERK1/2, Akt, and FAK pathways. *Cardiovasc. Res.* **115**, 463–475
27. McCall, A. S., Bhave, G., Pedchenko, V., Hess, J., Free, M., Little, D. J., *et al.* (2018) Inhibitory anti-peroxidasin antibodies in pulmonary-renal Syndromes. *J. Am. Soc. Nephrol.* **29**, 2619–2625
28. Kim, H. K., Ham, K. A., Lee, S. W., Choi, H. S., Kim, H. S., Kim, H. K., *et al.* (2019) Biallelic deletion of Pxdn in mice leads to anophthalmia and severe eye malformation. *Int. J. Mol. Sci.* **20**, 6144
29. Cartegni, L., Chew, S. L., and Krainer, A. R. (2002) Listening to silence and understanding nonsense: exonic mutations that affect splicing. *Nat. Rev. Genet.* **3**, 285–298
30. Landrum, M. J., Lee, J. M., Benson, M., Brown, G., Chao, C., Chitipiralla, S., *et al.* (2016) ClinVar: public archive of interpretations of clinically relevant variants. *Nucleic Acids Res.* **44**, D862–D868
31. Winter, J., Luu, A., Gapinske, M., Manandhar, S., Shirguppe, S., Woods, W. S., *et al.* (2019) Erratum: author correction: targeted exon skipping with AAV-mediated split adenine base editors. *Cell Discov.* **5**, 56
32. Liang, P., Sun, H., Sun, Y., Zhang, X., Xie, X., Zhang, J., *et al.* (2017) Effective gene editing by high-fidelity base editor 2 in mouse zygotes. *Protein Cell* **8**, 601–611
33. Kim, K., Ryu, S. M., Kim, S. T., Baek, G., Kim, D., Lim, K., *et al.* (2017) Highly efficient RNA-guided base editing in mouse embryos. *Nat. Biotechnol.* **35**, 435–437
34. Ryu, S. M., Koo, T., Kim, K., Lim, K., Baek, G., Kim, S. T., *et al.* (2018) Adenine base editing in mouse embryos and an adult mouse model of duchenne muscular dystrophy. *Nat. Biotechnol.* **36**, 536–539
35. Liu, Z., Lu, Z., Yang, G., Huang, S., Li, G., Feng, S., *et al.* (2018) Efficient generation of mouse models of human diseases via ABE- and BE-mediated base editing. *Nat. Commun.* **9**, 2338
36. Smith, D., Helgason, H., Sulem, P., Bjornsdottir, U. S., Lim, A. C., Sveinbjornsson, G., *et al.* (2017) A rare IL33 loss-of-function mutation reduces blood eosinophil counts and protects from asthma. *PLoS Genet.* **13**, e1006659
37. Tu, T., Song, Z., Liu, X., Wang, S., He, X., Xi, H., *et al.* (2022) A precise and efficient adenine base editor. *Mol. Ther.* **30**, 2933–2941
38. Tong, H., Wang, X., Liu, Y., Liu, N., Li, Y., Luo, J., *et al.* (2023) Programmable A-to-Y base editing by fusing an adenine base editor with an N-methylpurine DNA glycosylase. *Nat. Biotechnol.* **41**, 1080–1084
39. Chen, L., Zhu, B., Ru, G., Meng, H., Yan, Y., Hong, M., *et al.* (2022) Re-engineering the adenine deaminase TadA-8e for efficient and

specific CRISPR-based cytosine base editing. *Nat. Biotechnol.* **41**, 663–672
40. Cortes-Lopez, M., Chamely, P., Hawkins, A. G., Stanley, R. F., Swett, A. D., Ganesan, S., *et al.* (2023) Single-cell multi-omics defines the cell-type-specific impact of splicing aberrations in human hematopoietic clonal outgrowths. *Cell Stem Cell* **30**, 1262–1281.e8
41. Zhang, Y., Ge, X., Yang, F., Zhang, L., Zheng, J., Tan, X., *et al.* (2014) Comparison of non-canonical PAMs for CRISPR/Cas9-mediated DNA cleavage in human cells. *Sci. Rep.* **4**, 5405
42. Wu, Y., Liang, D., Wang, Y., Bai, M., Tang, W., Bao, S., *et al.* (2013) Correction of a genetic disease in mouse via use of CRISPR-Cas9. *Cell Stem Cell* **13**, 659–662
43. Prusky, G. T., Alam, N. M., Beekman, S., and Douglas, R. M. (2004) Rapid quantification of adult and developing mouse spatial vision using a virtual optomotor system. *Invest Ophthalmol. Vis. Sci.* **45**, 4611–4616
44. Umino, Y., Solessio, E., and Barlow, R. B. (2008) Speed, spatial, and temporal tuning of rod and cone vision in mouse. *J. Neurosci.* **28**, 189–198
45. Kretschmer, F., Sajgo, S., Kretschmer, V., and Badea, T. C. (2015) A system to measure the Optokinetic and Optomotor response in mice. *J. Neurosci. Methods* **256**, 91–105
46. Chen, D., Xu, T., Tu, M. J., Xu, J. L., Zhou, C. C., Cheng, L. L., *et al.* (2018) Recapitulating X-linked Juvenile retinoschisis in mouse model by knock-in patient-specific novel mutation. *Front. Mol. Neurosci.* **10**, 453